72nd International Astronautical Congress (IAC), Dubai, United Arab Emirates, 25-29 October 2021.

IAC–21–A6.4.4

Mitigation of Debris in LEO using Space-Based Lasers

Lewis Walker[a], Massimiliano Vasile[a]

[a]*Department of Mechanical & Aerospace Engineering,University of Strathclyde, James Weir Building, 75 Montrose Street, Glasgow, United Kingdom G11XJ*, lewis.walker@strath.ac.uk, massimiliano.vasile@strath.ac.uk

Abstract

Small (<10cm) debris fragments present a significant threat to all operational satellites in orbit. Although numerous strategies for debris mitigation have been proposed, most active space-based methods involve rendezvous maneuvers with targeted pieces of debris, making them unsuitable for the cleaning up of large populations of fragments. There are more appropriate for removing larger objects which are potential sources of further debris. Moreover, these types of strategies are inapplicable to fragments which are too small to be tracked from Earth which is a requirement for rendezvous. This paper extends previous work by the authors by focusing on the photon pressure case and using the previously developed models for investigating application to collision avoidance.

This paper investigates through numerical simulations the impact of an active debris mitigation strategy using space-based lasers, targeted at debris shells resulting from collision events. A realistic concept is proposed and modelled in detail using opportunistic interaction with debris, without rendezvous, and requiring zero knowledge of individual fragments' orbits from ground-based observations. The impact of the mission is simulated numerically by analyzing the dynamics of typical encounters and employing high-fidelity models of both photon pressure and laser ablation based interaction mechanisms.

The models are then adapted to the case of collision avoidance, which requires far less momentum transfer to achieve a meaningful displacement after several orbits.

Keywords: Asteroid flyby, Formation flying, Nanosatellite, LIDAR

1. Introduction

With space launch costs decreasing due to the advent of reusable rockets and cheap dedicated smallsat launch vehicles, the number of satellites in Earth orbit is likely to increase significantly over the coming years as space becomes more widely accessible. As the number of satellites grows, the risk of collisions and chain reactions thereof (the so-called Kessler syndrome) increases also, and so effective and feasible strategies must be developed to both prevent and respond to collisions and breakup events.

Satellite collision events, for example the 2009 Iridium-Kosmos collision, or deployment of anti-satellite weapons leave behind clouds of debris fragments which spread out due to nodal precession into shells [1] and slowly decay due to small amounts of atmospheric drag. If further collisions similar to the 2009 event were to occur, these debris shells could render particular orbital altitude bands unusable and highly dangerous to traverse until the population naturally deorbits. This is particularly problematic for higher orbits where the atmosphere is more sparse, and hence fragments take longer to decay. Due to the large numbers of fragments produced in such collisions, post-collision mitigation strategies involving rendezvous, capture, and deorbiting are impractical because of the huge propellant expenditure, making these strategies suitable only for the removal of defunct satellites or larger fragments which represent potential sources of further debris.

Laser based interaction offers the ability of interaction at a distance and without the necessity of rendezvous maneuvers. To date, proposed laser-based strategies employing photon pressure have been primarily ground-based, with the intention being collision avoidance over removal. These concepts, such as LightForce [2], employ one or several ground-based continuous-wave (CW) lasers which illuminate the target fragment with each pass overhead. These strategies require that the fragments are trackable from Earth and that their orbits be known in advance of interactions.

Space-based platforms have several advantages over

their ground-based counterparts. These are primarily due to the lack of atmospheric scattering, shorter range to target (resulting in higher fluence at target) particularly at higher orbits, and improved directionality of the applied force, with the net force vector being closer to the negative velocity direction. Ground-based platforms inherently suffer from a tradeoff between optimal beam alignment with the retrograde direction, and atmospheric depth traversed which causes greater attenuation. It is true however that some disadvantages of ground-based systems could be offset by simply constructing more powerful lasers on the ground, as their size, weight and power restrictions are far more generous.

As for ablation based strategies, L'ADROIT [3] is the most well-developed, space-based concept, where a single large satellite is proposed in an elliptical polar orbit between 560-960 km. L'ADROIT is rather similar to the concept proposed in this paper, utilizing an opportunistic interaction strategy with passing fragments rather than specific targets. However, the L'ADROIT concept as proposed does have some issues which this paper attempts to investigate. Firstly, the targeted altitude band, as will be discussed in this paper, has a relatively short natural lifetime for small fragments, making the potential return on investment limited. Secondly, the authors assumed the laser incidence direction to be perfectly aligned with the fragments' negative velocity vector, which is unrealistic and highly dependent on individual encounter dynamics. The authors also assumed the beam waist plane to be precisely aligned with the fragment longitudinally, implying both knowledge and tracking of the distance to the fragment, and a rapidly changeable variable focus beam. These may not be realistic assumptions and in this analyses we use a more realistic beam model to calculate laser fluence at the target.

2. Concept Overview

The proposed concept is as follows. The targeted population of debris is those fragments in the sub 10 cm size range - those which are both numerous and often too small to be accurately tracked from Earth. A small constellation of satellites is inserted into a shell around the Earth such that the constellation has access to all longitudes . The target altitude would be chosen such that the satellties reside in an altitude band which is particularly debris-dense.

Each satellite carries two primary instruments: a camera for acquisition and tracking of debris fragments, and a high-power continuous-wave (CW) laser, which is used to illuminate fragments and impart momentum. The concept was initially designed with CW lasers in mind, however pulsed operation is also modelled.

Due to the high power consumption of the laser system combined with an expected low overall duty cycle, the laser would be powered by a battery bank onboard the spacecraft, which would have sufficient capacity to power typical interaction events, and sufficient time between consecutive events to fully recharge with appropriately sized solar panels. This battery bank and solar array would also serve to power low-thrust electric propulsion for orbit maintenance or adjustments.

The camera onboard continually scans the sky behind the spacecraft, searching for fragments inside its field of view (FOV). When a fragment is identified, the laser is steered onto the target fragment to initiate an interaction, and tracks its movement across the sky. This is done without variable focusing to limit the mass of satellites and to not require knowledge of the range to the fragment. The aperture diameter of the lasers used in this concept is 20 centimetres - much smaller than that of other concepts - to reduce the mass of the steering related components and overall optical system. No prior knowledge of the fragments' orbits is assumed as the premise of the concept is to be able to interact with small, untrackable fragments. Thus, fragments are acquired and interacted with opportunistically, as they pass through the camera's FOV.

An additional use of the camera which in not studied here is to reconstruct the orbits of the debris fragments that are encountered. Since this concept is aimed at smaller, untracked fragments, this data alone provides valuable information relating to collision risk and avoidance.

Beyond the power system, no detailed attempt to estimate the size and mass of the individual spacecraft is made, however the author expects these would be of the small-sat class, and between 100 and 300 kilograms each. To launch a constellation of one hundred 300 kg satellites, two Falcon 9 launches would be required [4], costing $100 million with reused boosters. This assumes onboard thrusters are used to transfer from the delivery orbit to the operational orbit.

2.1 Lifetime Reduction from Small Velocity Changes

Since the net velocity change from photon pressure based interaction is expected to be small, an initial study was performed to assess the lifetime impact of small impulsive ΔV applications at varying altitudes. Since lower fragments naturally deorbit more quickly, it is expected that more meaningful lifetime reductions could be achieved for higher orbits. However, as the orbit gets higher, the spatial density of debris and the subsequent interaction rate would lower for a roughly uniform shell. Thus this class of mitigation strategy should be targeted at orbits that are high enough to

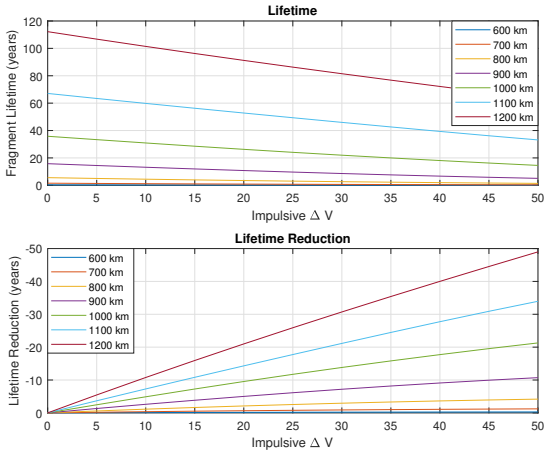

Fig. 1: Lifetime and lifetime reduction with an impulsive ΔV for circular, 45 degree inclined orbits of varying altitude

have relatively long lifetimes, while not being so high that the interaction rate becomes very low.

Orbits are propagated in this paper using a tool developed at the University of Strathclyde called CALYPSO. CALYPSO propagates orbits semi-analytically, taking into account perturbations including atmospheric drag, third body and J2-J4 perturbations. However, for the sake of computational efficiency, propagations in this paper are performed with drag as the only perturbation. For modelling atmospheric drag, the volume, size and area-to-mass ratio (AMR) of a 3D model of a 2cm aluminium hex nut are used to represent debris fragments. The AMR of this 3D model is 0.3391. This coincides approximately with the peak of the distribution of the catalogued debris from the Iridium-Cosmos collision [5].

Circular orbits of varying altitudes, inclined at 45 degrees were propagated until reentry. An initial impulsive ΔV was applied in the negative velocity direction ranging from zero to 50 ms^{-1}. The effects on the time-to-reentry can be seen in Figure 1.

It can be seen that, for higher orbits, a given ΔV application results in a larger absolute lifetime reduction, as expected. For lower orbits, the reduction becomes less meaningful - for example for 700 km altitude, the expected lifetime is already under 10 years, so smaller ΔV interventions may only reduce a fragment's life by a couple of months at best. Whereas for a 1200km orbit, smaller ΔV has a more significant impact, with only 10 ms^{-1} reducing lifespan by over 10 years.

Taking this into account, for the remained of this paper we consider a case of 1200km, 45 degree inclined orbits as the basis for feasibility assessment.

3. Debris Shell Characteristics

A debris population representative of that produced by a collision event must be generated to be used in this analysis. TLE data (obtained November 2020) is available for the tracked fragments from the 2009 Iridium-Cosmos collision, which can be compared with the pre-collision orbits of the two satellites to assess how the cloud characteristics compare with the orbit of the satellites.

It was found that the altitude and inclination followed approximately normal distributions, close to the pre-collision values of the satellties. Inclination was very tightly clustered around the pre-collision value, with standard deviations of 0.051^o for the Iridium-33 cloud and 0.0326^o for the Kosmos-2251 cloud. Altitude was found to have dissipated more over time due to differential drag effects, with standard deviations of 76.4 km and 79.0 km. The eccentricity distribution is observed empirically to follow a log-normal distribution, with no discernable relation between the satellite eccentricity and curve parameters. The right ascension of the ascending node and true anomaly had both dispersed to a quasi-uniform distribution [1].

For the modelling in this paper, a debris population was generated to simulate that which might be produced by the breakup of a satellite in a 1200 km circular orbit, inclined at 45 degrees, based on these distributions. Altitude and inclination were generated with a normal distribution with standard deviation equal to the average of those parameters from the Iridium-Cosmos clouds. Eccentricity was generated using a log-normal distribution with parameters equal to the average of those of the Iridium-Cosmos distributions, as both satellites were in near-circular orbits before the collision. The other orbital elements were generated as uniform random numbers between 0 and 359.9 degrees, assuming that the cloud has already spread into a shell.

4. Encounter Dynamics

In order to determine the long-term impact of this mission concept, a quasi-statistical approach must be used due to the computational demand of propagating thousands of fragments and computing their interactions with the spacecraft. To achieve this, a small, representative population of 632 fragments is propagated over a 10-year mission span, as well as the orbit of a single satellite. The slowly-changing equinoctal elements can then be interpolated for any instant of interest in the span, and converted to Cartesian to allow analysis of the encounter dynamics to be performed.

The separation between the spacecraft and any given fragment oscillates, producing many local minima over the span. These local minima in the separation, represent candidates for approach events, but require more processing to remove non-encounters and infeasible encounters. These candidate events are saved along with the states of the spacecraft and fragment at the instant of closest approach, in order to apply conditions in a decision tree to determine if camera acquisition - and subsequently laser interaction - may be possible in each event.

Feasible candidates are selected from the set by applying two conditions at the instant of closest approach - firstly, the fragment must be visible to the camera, and secondly, the fragment must be within 30 degrees of the spacecraft's negative velocity direction. Taken together, these ensure that the spacecraft and fragment are in similar orbits (large inclination differences would cause a high relative angular velocity and poor camera observability), and that the direction of the laser beam is reasonably well-aligned with the fragment's negative velocity direction (from the second condition). This also accounts for the limited field of view (FoV) of the camera.

The visibility condition is assessed by performing an SNR analysis using the camera system parameters and the distance to the object in a particular event. The limiting factor in the case of dim, moving objects is the image moving onto adjacent pixels before the required SNR can be reached. The condition for visibility then becomes that the required SNR must be achievable before the object image moves by one pixel width in the sensor plane.

The relative angular velocity of the downselected events must now be calculated. Let $\underline{S}$ be the separation vector originating at the spacecraft and ending at the fragment. Let $\underline{V_R}$ be the velocity of the fragment relative to the satellite. $\underline{V_R}$ has a component perpendicular to $\underline{S}$, which we shall call $\underline{V_P}$, where $\|\underline{V_P}\| = \sin(\phi)\|\underline{V_R}\|$, where ϕ is the angle between $\underline{S}$ and $\underline{V_R}$. At the instant of closest approach - where the relative angular velocity will be highest - the angular velocity can be found geometrically (Equation 1).

$$\frac{d\theta}{dt} = \frac{\|\sin(\phi)\underline{V_R}\|}{\|\underline{S}\|} \tag{1}$$

4.1 Optical Acquisition

Analysis on optical acquisition is performed by estimating the SNR of pixels containing the fragment compared with background pixels. SNR is here defined as the ratio of the mean signal photon count on a pixel containing the fragment (μ_s), to the standard deviation of the noise counts in background pixels (σ_n) (Equation 2.

$$SNR = \frac{\mu_s}{\sigma_n} = \frac{\mu_s}{\sqrt{\mu_n}} \tag{2}$$

The expected, or mean, signal photon count per pixel per exposure, μ_s, can be derived from first principles and written as

$$\mu_s = \frac{\Phi_\odot \Delta\lambda A_F \alpha_F \lambda A_{col} \eta_c}{2\pi R^2 hc n_{px}} t_{exp} \tag{3}$$

Where $\Phi_\odot$ is the solar irradiance in $Wm^{-2}nm^{-2}$, $\Delta\lambda$ is the bandwidth of the camera, A_F is the illuminated surface area of the fragment visible to the spacecraft, α_F is the albedo of the fragment in the chosen wavelength band, λ is the central wavelength of the CCD's sensitive band, R is the distance to the fragment, h is Planck's constant, A_{col} is the area of the light collecting optic, η_c is the overall photon-to-electron conversion efficiency of the entire camera-CCD system, t_{exp} is the exposure duration, and $n_{px,i}$ is the number of pixels that the object's image is spread across, which is the point spread function (PSF) for sub-pixel sized sources as will be the case in this scenario.

Background, or noise, counts in a CCD typically consist of several sources - dark counts, non-image photons in the field of view, and readout noise. In this case, we assume negligible non-image photons, as observations will not be made while the Sun is in the field of view, the aperture would have a sun-blocking baffle, and the camera will be kept pointed above the horizon, with the Earth also outside of the field of view. Thus the noise is dominated by dark noise and readout noise. The mean noise photon count *per pixel* can be written as

$$\mu_n = Dt_{exp} + R \tag{4}$$

Where D is the mean dark count rate per pixel, and R is the mean readout noise per pixel per exposure. In space-based CCD imagers, sub-100 Hz/px dark count rates have been demonstrated with active cooling, with around 10 Hz/px being achievable at temperatures of -30 Celsius [6]. Given the large capacity power delivery and storage systems that will be required for the laser system on board each satellite for this mission, it is reasonable to assume CCD active cooling will be available to reduce dark count rate to the 10 Hz/px level, so this is the level used in the base case calculations.

A binary number indicating if the two conditions are fulfilled at a given instant in the encounter can be calculated by comparing the relative angular velocity at a given instant in the encounter with the minimum required exposure for a given SNR. An example of this can be seen in Figure 2, with the orange line indicating when the conditions are fulfilled.

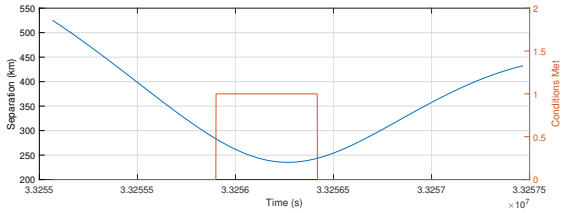

Fig. 2: Example of information extracted on the dynamics of a single encounter. The orange curve (right axis) is the binary condition where 1 denotes the fragment is observable at that instant. The full states of both the satellite and fragment are extracted from each encounter.

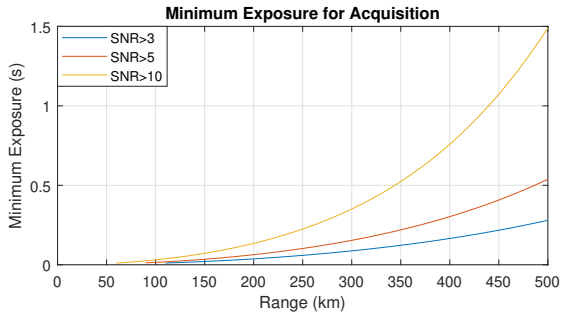

Fig. 3: Minimum required exposure at a given range to achieve the specified SNR.

Figure 3 shows the minimum required exposure for SNR 3, 5, and 10 as a function of distance from the fragment, using the parameters in Table 1, which are the assumed camera parameters for this analysis.

Using the above data, it is possible to determine if a fragment is observable at a specific point in any encounter event.

Parameter	Value
Circular Aperture Diameter	20 cm
Fragment Albedo	0.5
Camera Efficiency	40%
Bandwidth	350 nm
Solar Irradiance	1.5 $\mathrm{Wm^{-2}nm^{-1}}$
Debris Illuminated Area	2.034e-4 m^2
PSF	4 pixels
Central Wavelength	550 nm
Exposure Duration	0.1339 seconds
Dark Count Rate	10 hz $\mathrm{px^{-1}}$
Mean Read Noise	5 counts $\mathrm{exposure^{-1}}$ $\mathrm{px^{-1}}$

Table 1: Parameters used in imaging SNR analysis

The illuminated area chosen in these calculations was was that of the 3D model of the hex nut, along the direction of the axis passing through the central hole.

From the analyses in this section it is also possible to extract information on the rate of interaction. Timestamps of all viable interactions were used to obtain the distribution of the time between consecutive events. The mean time between events is 41802 seconds, or on average 0.483 encounters per day. When scaling up from the smaller population of 632 fragments to a more realistic population of 5000, the expected event rate is approximately 4 encounters per day. This high encounter rate suggests that the rate of interaction is likely to be limited by the power system and not the encounter dynamics.

5. Laser Interaction Model

In order to precisely quantify the force being applied to the fragment, a high fidelity model of photon pressure over 3D shapes was developed. The model takes a user-defined 3D model of a debris fragment, triangulates the surface and calculates the net laser pressure force and torque vectors at each timestep. This is used to update the velocity and rotation state with each timestep, and incrementally integrate the impulse over the course of the interaction to obtain the net momentum transfer vector.

5.1 Element Illumination

After the 3D model has been triangulated, the illumination state I of each element must be determined to allow force calculation. This effectively modifies the area of the element to account for full, zero, or partial illumination. First, back face culling is applied by setting $I = 0$ for all elements where $\hat{\mathbf{n}} \cdot \hat{\mathbf{i}} > 0$, where $\hat{\mathbf{n}}$ is the element's normal vector and $\hat{\mathbf{i}}$ is the direction of the incident light. Then, occluded vertices are detected by searching for intersections between any other element and the direction $-\hat{\mathbf{i}}$, originating at the vertex in question. For each element with $I > 0$ after back-face culling, an illumination state is assigned depending how many of the three vertices are illuminated. For example, if no vertices are illuminated, $I = 0$, and if two are illuminated then $I = \frac{2}{3}$.

5.2 Photon Pressure Force

When light is incident on a surface, some fraction is absorbed and the remainder is reflected. The reflected component can be further divided into diffuse and specular components - in diffuse reflection, photons are scattered in all directions due to surface imperfections. In specular reflection, distinct rays of light reflect from the surface like a mirror, obeying Snell's law. For metallic space debris, the

specular component is likely to be non-negligible. In order to accurately calculate the net momentum transfer, all three components should be modelled and their respective force components simulated.

$$\mathbf{F}_e = S\mathbf{F}_{specular} + (1-S)\mathbf{F}_{isotropic} + \mathbf{F}_{absorption} \quad (5)$$

Where S is a specularity factor between 0 and 1 which determines the fraction of light that is reflected specularly. For isotropic diffuse reflection the rate of momentum transfer for each direction of reflected light must simply be integrated over 180 degrees. All transverse components cancel so only the surface-normal components need be integrated. Upon completing this integration, the relation in Equation 6 is obtained.

$$\mathbf{F}_{isotropic} = -\frac{2\alpha P_{laser} I A_s}{\pi c}\hat{\mathbf{n}} \quad (6)$$

where $A_s = A(\hat{\mathbf{n}} \cdot \hat{\mathbf{i}})$ is the area of the surface presented to the direction of the light source, in this case the presented area of each surface element of the triangulated mesh. A is the full area of the element, α is the albedo of the material, $\hat{\mathbf{n}}$ is the unit normal vector of the surface element, P_{laser} is the power per unit area of incident light and c the speed of light.

For the specular component, the net force is equal to

$$\mathbf{F}_{specular} = -\frac{\alpha P_{laser} I A_s}{c}\hat{\mathbf{r}} \quad (7)$$

where $\hat{\mathbf{r}}$ is the unit vector of the direction of the reflected light. The force on the surface element due to absorption is

$$\mathbf{F}_{absorption} = \frac{(1-\alpha) P_{laser} I A_s}{c}\hat{\mathbf{i}} \quad (8)$$

where $\hat{\mathbf{i}}$ is the direction of the incident light.

The algorithm finds the total force for each surface element and the sum to find the net force on the object at each timestep:

$$\mathbf{F}_{net}(t_i) = \sum_{e=1}^{N} \mathbf{F}_e(t_i) \quad (9)$$

where t_i denotes timestep i, N is the total number of elements in the 3D model and $\mathbf{F}_e$ if the net force on element e calculated using Equations 5-8.

Torque is calculated by taking the cross product $\mathbf{F}_e \times \mathbf{R}_e$, where $\mathbf{R}_e$ is the vector connecting each element's center (mean of the vertices) to the object's center of mass.

For propagation to the next timestep, the object's current velocity, angular velocity magnitude and instantaneous axis of rotation are updated from the net force and net torque. The equation for angular velocity update is

$$\omega_i = \omega_{i-1} + \dot{\omega}_{i-1} dt \quad (10)$$

where τ_i is the net torque vector at timestep i, dt is the timestep size, ω_i is the angular velocity vector at timestep i, and

$$\dot{\omega}_{i-1} = \frac{\tau_i}{\hat{\mathbf{a}}\mathbf{I}\hat{\mathbf{a}}^T} \quad (11)$$

where

$$\hat{\mathbf{a}} = \frac{\tau_i}{\|\tau_i\|} \quad (12)$$

is the instantaneous axis of angular acceleration, $\mathbf{I}$ is the inertia tensor of the 3D model, and the denominator of Equation 11 is the moment of inertia along the direction $\hat{\mathbf{a}}$.

5.3 Longitudinal Laser Profile

For a Gaussian, near-single-mode beam, divergence reaches its minimum possible value of $\theta_d = M^2 \frac{\lambda}{2\pi w_0}$, where λ is the laser wavelength and w_0 is the beam waist radius - the radius of the most tightly focussed point along the beam axis. The factor M^2 (greater than or equal to 1), known as the beam quality factor, is added to this expression to capture any deviation from the theoretical minimum, perfectly Gaussian beam profile.

From this, simple geometry allows the beam radius $w(R)$ at any given longitudinal distance from the focal plane (or beam waist) to be calculated according to Equation 13, where R is the distance from the emitter and z_0 is the focal plane's distance from the emitter - thus the term in brackets is the distance of the point of interest from the focal plane. w_0 is the waist radius.

$$w(R) = w_0 + \sqrt{(R-z_0)^2}\tan(\theta_d) \quad (13)$$

This section will discuss optimizations of the focal plane location and waist radius to increase the irradiance delivered to fragments during interaction.

The simplest approach would be to simply have the waist radius at the emitter, or $z_0 = 0$. However, since this concept deals with long ranges and the effect of the interaction depends heavily on the irradiance of illumination of a fragment, alternatives should be explored that allow for higher irradiance to increase effectiveness and/or reduce laser requirements. Agile, variable-focus optics are not assumed to be available on the spacecraft due to mass and size restrictions.

It is important to note that z_0 cannot be freely chosen, but is constrained by the maximum size of the emitter on board

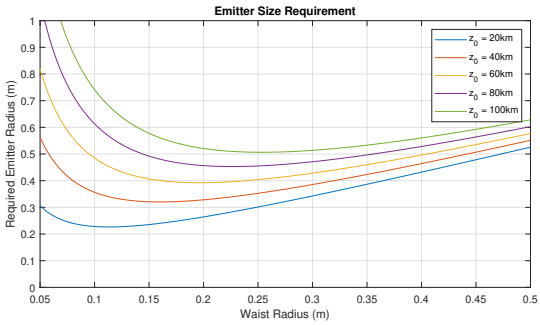

Fig. 4: Emitter size requirement for various z_0 and w_0

the spacecraft. The required emitter radius can be obtained from Equation 13 by setting $R = -z_0$. Figure 4 shows the relationship between desired waist radius and required emitter size, with z_0 fixed at several values.

It can be seen that larger emitters allow the waist to be placed further away from the craft, and thus a higher fluence to be delivered to the target. A constraint on the size of the emitter must exist since it must fit on board the spacecraft, but precisely defining this is outwith the scope of this paper. An approximate upper limit of $w_e = 0.1$ m was chosen to constrain the parameters z_0 and w_0. Since long distance interactions are required, it is desirable to have the focal plane as far from the spacecraft as possible for a given emitter size to maximize the fluence at the target. From Figure 4, z_0 should be lowered just until the curve touches the upper limit of $w_e = 0.1$, giving the best-case optimization of the laser profile. The optimal focal plane distance was found to be $z_0 = 15.59$ km with a waist radius $w_0 = 0.1$ m. These optimal parameters are used in the laser-debris interaction modelling in later sections.

5.4 Impulse Transfer Calculation

Photon Pressure

The database of encounter dynamics obtained in Section 4 is now used to model the interaction of the laser beam with the fragment and obtain a net impulse transfer for each encounter. A total of 7549 viable encounters were extracted from the orbital propagation and used to build this database.

An example of the dynamics extracted from a single encounter can be seen in Figure 2, where the orange line is a binary state of observability (all criteria being met) for that instant in time. Thus, only the dynamics during periods where this condition equals 1 are fed into the photon pressure model. The distribution of visibility window duration can be seen in Figure 5.

The separation vectors $\mathbf{S}(t)$ during the observable window for each encounter are passed into the laser-debris interaction (LDI) model described previously. This integrates the laser pressure force over the course of the interaction, accounting for variability in the direction of incidence and magnitude of irradiance over time.

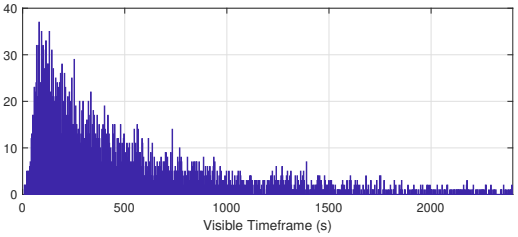

Fig. 5: Distribution of visibility window duration

The LDI model outputs a net impulse vector which represents the net momentum transfer of the entire interaction. To facilitate generation of new encounters according to the found distributions, the direction of the impulse is converted from Earth-centric 3D coordinates to a local reference frame for each encounter. This sets the origin at the fragment position at the distance-weighted central time of the observability window. A local instantaneous reference frame is defined which allows the net impulse direction to be expressed in terms of its magnitude, declination and right ascension relative to the negative velocity direction.

Building this large database allows encounters to be 'generated' by selecting random encounters from the database, and applying an impulsive ΔV to different fragment states in its own local reference frame. Using this method ensures that any complex correlations between the dynamics of the encounter and the resultant net impulse are preserved, while still being fast to compute by not requiring the LDI model or orbit propagation to be used for every encounter.

6. Long Term Mission Impact Modelling

Using the results of all previous sections, we are now able to assess the long-term impact of a constellation of satellites deployed into a debris shell as a response to a breakup event.

To achieve this, a new set of 5000 fragments is generated in the same way as before, centered around the same 1200 km altitude.

Interaction times are generated using the same distribution of consecutive event separations found earlier in the representative population, scaled up to the larger population, until a full 10-year mission duration's worth of encounters has been generated for a single satellite. For each interaction, a random fragment identifier number is assigned, which is the fragment that is encountered in that instance.

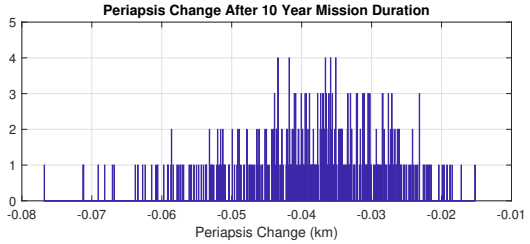

Fig. 6: Net change in periapsis for 10 year mission duration using photon pressure

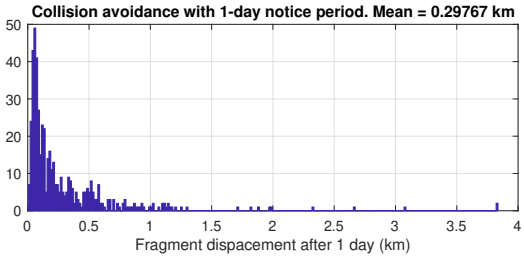

Fig. 7: Fragment displacement w.r.t unperturbed position after 1 day (500 encounters).

This is repeated for each satellite in the constellation - 100 in the base case - and all events together with their timestamps, fragment identifiers and satellite identifiers are collated into a single database. Exactly half of these events are then randomly selected and removed, to account for eclipse conditions where the Sun does not illuminate the fragment, rendering it invisible to the camera. Finally, for consecutive events involving the same spacecraft where the time separation is insufficient to recharge the batteries using solar power, only the first encounter is kept.

Fragments' orbits are then individually propagated from $t = 0$ to each subsequent interaction time. Here, an impulsive ΔV - whose magnitude and relative direction are taken from a randomly selected at encounter from the database built in Section 5.4 - is applied to its state vector before it is propagated to the next encounter. After the final encounter has been reached, the fragment's orbit is then propagated to the end of the 10 year mission span with no further interaction perturbations. The original orbit is also propagated unperturbed for the full 10 year duration to identify changes due to the applied interactions. During these propagations, for the sake of computation time, the only perturbation in the orbit propagation is atmospheric drag - J2 and other perturbations are disabled.

6.1 Results for Orbit Lowering

Figure 6 shows the distribution of periapsis change for each fully propagated fragment in the population. In these results, only 417 fragments have been propagated to the end of the 10 year mission duration to gain an insight into the expected effect on any given fragment in the population. As can be seen, the expected change in periapsis is small, with a mean reduction of only 38.6 metres. Lifetime reduction was assessed and found to be negligible. This result indicates that photon pressure is not a viable mechanism by which to lower the orbit of debris fragments using a space-based platform. However, application of impulse via laser ablation is a much more efficient method and will be studied in future work for use in this mission concept.

7. Adaptation for Collision Avoidance

Despite the poor potential to lower a fragment's orbit via photon pressure, the constellation based approach may still have some application for collision avoidance, which allows a very small perturbation to a fragment's velocity to compound over time, resulting in a large position change.

To investigate this possibility, random fragments were selected from the population used previously and propagated for some shorter time t, both with and without a single impulsive interaction applied at $t = 0$ in order to assess the magnitude of the effect by comparing the position of the fragment at the end of the propagation period. The results of this for 500 different fragments and impulsive interactions after a 1 day collision notice period can be found in Figure 7. With only a single interaction, for the chosen laser parameters and this fragment's area-to-mass ratio, it is possible to achieve an along-track displacement of several hundred metres with one day of advance notice of a collision.

This analysis was repeated for several different notice periods. The results of this can be found in Figure 8, showing that with sufficient notice period, a displacement of several kilometres w.r.t the unperturbed position could be achieved.

Figure 9 shows the distribution of the angle of the deviation with respect to the fragment's negative velocity vector after one day, showing tight clustering around zero, indicating that the fragments are being temporally displaced to avoid a potential collision.

8. Ablative Interaction

Due to the poor orbit-altering effect found previously with photon pressure, ablation was investigated as an alternative mode of interaction using the same mission architecture. In ablative coupling, momentum is transferred to the target object by vapourizing a small amount of surface material by use of high-energy laser pulses. The expanding plume of gas and plasma then produces a force on the fragment. The strength of this coupling in Newtons per joule has

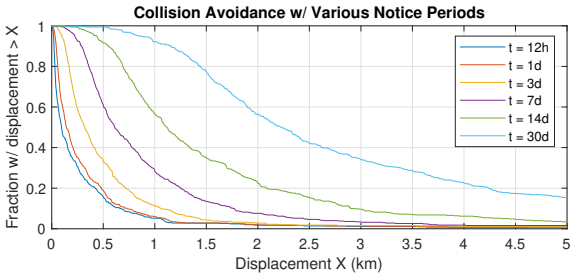

Fig. 8: Fraction of fragments where a minimum displacement is achieved after various notice periods up to 30 days.

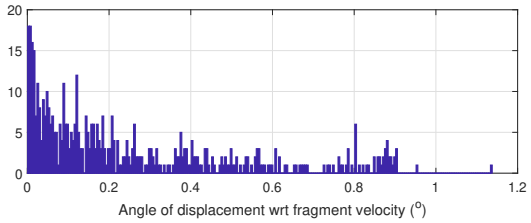

Fig. 9: Relative angle of displacement showing clustering in the along-track direction. 1 day notice period, 500 encounters.

the potential to be several orders of magnitude stronger than that of photon pressure with sufficient energy and power density on the target surface.

Impulse transfer is integrated element-wise similarly to the photon pressure model, according to Equation 14 where each element is denoted by e.

$$\Delta \mathbf{p}_e = A_e \Phi_e C_m(\Phi_e) \hat{\mathbf{n}}_\mathbf{e} \tag{14}$$

Here, A_e is the element area, Φ_e is the energy density on element e, dependent on the distance from the emitter, and $C_m(\Phi_e)$ is the momentum coupling coefficient. For $C_m(\Phi_e)$, the empirical curve from [7] was shifted such that the peak occurred at the average optimal fluence from all available data in the literature for aluminium in vacuum at the relevant pulse duration [8, 9, 7, 10]. The C_m curve used can be seen in Figure 10.

Using this model, the same set of encounter dynamics were used to calculate a set of net impulse transfer vectors in the ablation case. For each interaction, 300 3 kJ pulses were simulated, applied consecutively at a rate of 25 Hz, at a random time point within the visibility window as no assumption is made of range knowledge which could be used to maximize the fluence.

From here, the same mission simulation method as before is followed, drawing impulsive interactions from the newly generated ablative interaction set.

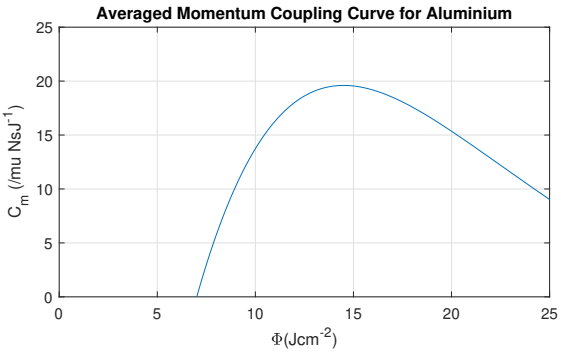

Fig. 10: Momentum coupling curve used in the ablation impulse transfer model obtained from averaged literature nanosecond pulse results

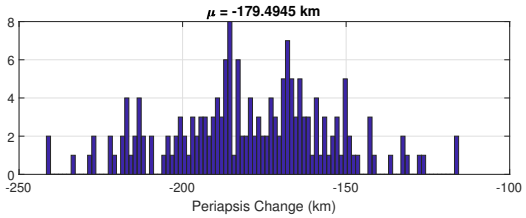

Fig. 11: Periapsis change for propagated fragments in the ablation case

8.1 Ablation Results

A sub-population of 177 fragments was propagated for the same 10 year mission duration to determine the impact of the intervention. Due to the stronger momentum coupling, as expected this mode of interaction induced a much stronger effect on fragments' orbits and lifetimes than the photon pressure case. Results for the change in periapsis and lifetime can be found in Figures 11 and 12 respectively. It can be seen that in the ablation case, the lifetime reduction is measured in decades and periapsis reduction of over 100 km is achieved in all cases.

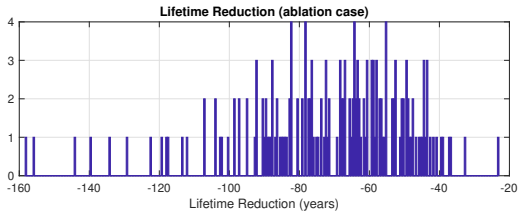

Fig. 12: Lifetime change for propagated fragments in the ablation case. Some fragments have already re-entered in the 10-year mission span.

9. Discussion and Conclusion

In this paper, detailed modelling of a new concept for space debris mitigation using space-based laser pressure was performed to determine the feasibility of reducing the lifetime of a large population of small debris fragments. The results of these analyses indicate that photon pressure is not a viable mechanism by which to attempt orbit lowering of debris using a space-based platform. The achieved reduction in periapsis was less than a standard deviation from zero, and so the effect was negligible even for a 100-satellite constellation carrying 10kW CW lasers.

The concept was subsequently adapted and re-modelled using ablative interaction with pulsed lasers, leading to a far stronger effect on the orbits of fragments in the shell. Using ablation, it is possible to achieve lifetime reduction of decades for fragments in orbits with 1200 km altitude, which could significantly reduce the risk posed by debris shells left behind after collision events at these altitudes.

Importantly, we have shown that it is indeed possible to optically acquire small (2 cm) fragments of debris in orbit using a small camera without prior knowledge of the fragments' orbits. This is dependent on the exact dynamics of the encounter, but is possible in a high number of encounters where the fragment and spacecraft are on similar orbits.

Subsequent analysis in this paper showed the potential for this concept to be adapted for collision avoidance, with an along-track displacement of several kilometers being achievable one day after the interaction. One could envision this being used in combination with the proven optical acquisition in a campaign of orbit determination for a large population of small fragments. Gaining knowledge of their orbits could allow the identification of future collision events and allow interventions to be performed using the same platform to prevent such collisions. This leaves open the potential for future work on the determination of fragment orbits using angles-only camera data achieved from these individual flybys.

Acknowledgements

The work in this paper was supported and funded by Fraunhofer UK Centre for Applied Photonics and the University of Strathclyde.

References

[1] Carmen Pardini and Luciano Anselmo. "Physical properties and long-term evolution of the debris clouds produced by two catastrophic collisions in Earth orbit". In: *Advances in Space Research* 48.3 (2011), pp. 557–569.

[2] Fan Yang Yang et al. "LightForce photon-pressure collision avoidance: Efficiency analysis in the current debris environment and long-term simulation perspective". In: *Acta astronautica* 126 (2016), pp. 411–423.

[3] Claude R Phipps. "L'ADROIT–A spaceborne ultraviolet laser system for space debris clearing". In: *Acta Astronautica* 104.1 (2014), pp. 243–255.

[4] SpaceX. *Falcon 9 Capabilities and Services*. Retrieved: May 2021.

[5] Ting Wang. "Analysis of Debris from the Collision of the Cosmos 2251 and the Iridium 33 Satellites". In: *Science & Global Security* 18.2 (2010), pp. 87–118.

[6] Olivier Gilard et al. "CoRoT satellite: analysis of the in-orbit CCD dark current degradation". In: *IEEE transactions on nuclear science* 57.3 (2010), pp. 1644–1653.

[7] Bin Wang. "Laser ablation impulse generated by irradiating aluminum target with nanosecond laser pulses at normal and oblique incidence". In: *Applied Physics Letters* 110.1 (2017), p. 014101.

[8] Claude R Phipps et al. "Measurements of laser impulse coupling at 130 fs". In: *High-Power Laser Ablation V*. Vol. 5448. International Society for Optics and Photonics. 2004, pp. 1201–1209.

[9] Claude R Phipps et al. "Laser impulse coupling measurements at 400 fs and 80 ps using the LULI facility at 1057 nm wavelength". In: *Journal of Applied Physics* 122.19 (2017), p. 193103.

[10] DucThuan Tran et al. "Impulse and mass removal rate of aluminum target by nanosecond laser ablation in a wide range of ambient pressure". In: *Journal of Applied Physics* 122.23 (2017), p. 233304.